AMERICAN
METEOROLOGICAL
SOCIETY

Journal of the Atmospheric Sciences

The DOI for this manuscript is doi: 10.1175/JAS-D-18-0131.1

The final published version of this manuscript will replace the preliminary version at the above DOI once it is available.

If you would like to cite this EOR in a separate work, please use the following full citation:

Tang, X., Z. Tan, J. Fang, E. Munsell, and F. Zhang, 2018: Impact of the Diurnal Radiation Contrast on the Contraction of Radius of Maximum Wind during Intensification of Hurricane Edouard (2014). J. Atmos. Sci. doi:10.1175/JAS-D-18-0131.1, in press.

Impact of the Diurnal Radiation Contrast on the Contraction of Radius of Maximum Wind during Intensification of Hurricane Edouard (2014)

Xiaodong Tang[1], Zhe-Min Tan[1], Juan Fang[1], Erin B. Munsell[2,3], and Fuqing Zhang[4]

[1]Key Laboratory of Mesoscale Severe Weather, Ministry of Education, and School of Atmospheric Sciences, Nanjing University, Nanjing, China

[2]Laboratory for Mesoscale Atmospheric Processes, NASA Goddard Space Flight Center, Greenbelt, Maryland, USA

[3]Universities Space Research Association, Columbia, Maryland, USA

[4]Department of Meteorology, and Center for Advanced Data Assimilation and Predictability Techniques, The Pennsylvania State University, University Park, Pennsylvania, USA

Submitted to *Journal of the Atmospheric Sciences* for publication as an article

Revised on 31 October 2018

Corresponding author contact: Xiaodong Tang, Ph. D., School of Atmospheric Sciences, Nanjing University, 163 Xianlin Avenue, Nanjing 210023, P. R. China

Email: xdtang@nju.edu.cn

Abstract

This work examines the impacts of the diurnal radiation contrast on the contraction rate of the radius of maximum wind (RMW) during intensification of Hurricane Edouard (2014) through convection-permitting simulations. Rapid contraction of RMW occurs both in the low- and mid-levels for the control run and the sensitivity run without solar insolation, while the tropical cyclone contracts more slowly in the low-levels and later in the mid-levels and thereafter fails to intensify continuously in the absence of the night phase, under weak vertical wind shear (~4 m s^{-1}). The clouds at the top of the boundary layer absorbs solar shortwave heating during the daytime, which enhanced the temperature inversion there and increased the convective inhibition, while nighttime destabilization and moistening in low-levels through radiative cooling decrease convective inhibition and favor more convection inside the RMW than in the daytime phase. The budget analysis of the tangential wind tendency reveals that the greater positive radial vorticity flux inside of the RMW is the key RMW contraction mechanism in the boundary level at night, due to the enhanced convection. However, the greater positive vertical advection of tangential wind inside of the RMW dominates the RMW contraction in the mid-levels.

1. Introduction

"Convective ring theory" (Shapiro and Willoughby 1982; Willoughby et al. 1982) hypothesizes that in response to sustained condensational heating in the tropical cyclone (TC) eyewall updrafts, both contraction of the radius of maximum wind (RMW) and intensification occur. The eyewall convective heating drives a secondary circulation. Assuming a TC is restored toward thermal wind balance, the tangential wind tendency tends to be greater inside of the RMW than at the RMW itself, which is diagnosed using the Sawyer–Eliassen equation. Therefore, the RMW will contract as the TC intensifies. The RMW contraction can be understood as a result of an increasing negative radial gradient of tangential wind tendency inward of the RMW in the kinematic framework used by Stern et al. (2015). Recent idealized numerical simulations of TCs and observations of real cases further show that most of the contraction typically occurs prior to a storm's primary intensification stage (Stern et al. 2015; Kepert 2017). During the early stage before rapid intensification (RI) onset, the symmetric component of Tropical Storm Earl (2010) was shallow, broad, and diffuse (Rogers et al. 2015). The TC had an asymmetric distribution of convection when it was experiencing moderate shear. The early intensification stage is further identified, which is represented by a distinct eyewall contraction in Typhoon Vicente (2012) (e.g. Chen et al. 2017). Although contraction and intensification could begin at the same time, contraction ceases long before peak intensity is achieved (Stern et al. 2015).

Observations and numerical simulation studies show that the diurnal radiation contrast can influence TC genesis, intensity and structure changes (Dunion et al. 2014;

Melhauser and Zhang 2014; Tang and Zhang 2016, hereafter TZ16; Navarro and Hakim 2016; Tang et al. 2017, hereafter T17; Navarro et al. 2017; O'Neill et al. 2017). The environmental stability and the intensity of deep moist convection in TCs can be considerably modulated by the diurnal extremes in radiation (Melhauser and Zhang 2014). Furthermore, the responses to the diurnal cycle of net radiation forcing and the impacts on structure and intensity were found to be different in extent and feature throughout the different stages of TCs through comparisons between sets of sensitivity experiments (TZ16; T17). In general, nighttime destabilization of the local and large-scale environment through radiative cooling may promote deep moist convection and increase the genesis potential at the formation stages of TCs (Melhauser and Zhang 2014; TZ16). TZ16 found that during the mature stage of TCs, the net radiative cooling at nighttime mainly increases the convective activity outside of the eyewall that leads to broader/stronger rainbands and larger TC size in terms of the radius of azimuthally averaged surface wind speed of 34 kt. However, there is no consensus in the literature on the role of the diurnal radiation contrast on TC vortex wind structure and intensity. In particular, it remains unexplored how the diurnal radiation contrast affects RMW contraction during TC intensification, which will be the focus of the current study. Dynamical or thermodynamic explanations for impact of the diurnal radiation contrast on the RMW contraction will be investigated further from a kinematic perspective through analysis of numerical simulations of Hurricane Edouard (2014).

The remainder of this paper is organized as follows. The model settings and experimental design are described in section 2. An overview of Edouard (2014) and the associated numerical simulation are given in section 3. Radiative effects on the RMW contraction rate during intensification will be presented in section 4. Finally, a discussion and the conclusions follow in section 5.

2. Model settings and experimental design

The Advanced Research version of the WRF Model (ARW) (Skamarock et al. 2008) was employed to perform a control simulation (CNTL) and sensitivity experiments. The model domains are triply nested through two-way nesting with horizontal resolutions of 27, 9, and 3 km (Fig. 1a). The two inner domains (D02 and D03) are vortex following. The following physics parameterizations were used in this study: the Dudhia shortwave radiation scheme (Dudhia 1989), the Rapid Radiation Transfer Model (RRTM) longwave radiative scheme (Mlawer et al. 1997), the WRF single-moment 6-class microphysics scheme (Hong and Lim 2006), the Yonsei University (YSU) scheme for the planetary boundary layer (BL) (Hong et al. 2006), and the Grell–Freitas cumulus scheme (Grell and Freitas 2014) in the outermost 27-km mesh. The 1-D ocean mixing layer model (Pollard et al. 1972) coupled with WRF was also employed. The details of the model physics configuration and initialization processes can be found in Zhang and Weng (2015), Weng and Zhang (2016), and Munsell et al. (2017). An endless daytime simulation with the solar insolation set at local noon (“ConstSolarRad”) and an endless nighttime simulation with no solar insolation (“NoSolarRad”) are conducted, starting at 48 model integration hours of the control simulation (the ConstSolarRad48h and NoSolarRad48h experiments in TZ16, their Table 1), which includes the focused process of RMW contraction in the CNTL experiment (Fig. 1d).

The TC center was defined as the centroid of sea level pressure in the following analysis, which was calculated within a circular region representing the size of the TC inner core. The pressure centroid represents the storm center well, especially for weaker and more asymmetric TCs, since the method consistently places the TC center within the region of weak storm-relative wind and produces a smooth variation of vortex tilt in magnitude and direction (Nguyen et al. 2014). Therefore, this method for identifying the TC center was recommended to be adopted in the study for early development and intensification stage of TC (Chen et al. 2017, 2018).

3. Overview of Edouard (2014) and the associated numerical simulation

Edouard was designated as a named tropical depression over the far eastern tropical Atlantic by 1200 UTC 11 September 2014 (Stewart 2014) (Figs. 1b, c). While it moved to the northwest, over the period from about 0000 UTC 14 September to 0000 UTC 15 September the maximum 10-m sustained winds increased by 25 knots (i.e. 12.9 m s^{-1}). Edouard reached a peak intensity of 54 m s^{-1} as a major hurricane at 1200 UTC 16 September. The control run replicates the general features of development in all stages of the lifetime mentioned above, including the processes of RMW contraction and intensification (Figs. 1b, c, d). Although the intensifying rate does not meet the NHC criteria (15.4 m s^{-1} in 24 hour) of RI in the best-track data, 1200 UTC 14 September can be considered as RI onset according to the time evolution of maximum 10-m wind speed of CNTL (Fig. 1b). Moreover, the storm intensity increases nearly 30 m s^{-1} over the succeeding 48 hours in CNTL (Fig. 1b). The RMW of CNTL and

NoSolarRad both began to contract rapidly 24 hours before RI onset, consistent with that from the best-track data, while the ConstSolarRad shows a larger fluctuation in RMW after the 0000 UTC 14 September (Fig. 1d). Moreover, rapid contraction of the RMW occurs both in the low- and mid-levels for NoSolarRad (Figs. 2a, c), while the RMW contracts more slowly in the low-levels and later in the mid-levels and thereafter fails to intensify continuously in ConstSolarRad (Figs. 2b, d). The following section will explain the impact of the diurnal radiation contrast on the RMWl contraction and intensification of Edouard, using the two sensitivity experiments of NoSolarRad and ConstSolarRad for clean comparisons.

4. Radiative effects on eyewall contraction and RI

a. Radiative impacts on convection

The most vigorous and intense convection and vertical updrafts are found between 30-90 km radius in NoSolarRad (Fig. 2c). Figure 3 shows that in this area there were fewer clouds at the heights of 3-10 km before the RI onset (Figs. 3a and 3b), while relatively more low clouds existed at the top of the boundary layer[1] (BL) than those in the mid-layers. The clouds at the top of the BL absorbed solar shortwave radiation at daytime and heated this level most (Fig. 3c), while longwave radiation produced some cooling there (Fig. 3f). Consequently, net radiation more significantly heated the BL top in ConstSolarRad (Fig. 3e); the 18-hours integrated contribution of which to

[1] The thermodynamic definition of boundary layer is adopted here following Powell (1990), characterized by the layer in which the potential temperature (or virtual potential temperature) is appreciably well mixed. The height of boundary layer in the TC inner core is below 1 km in the study.

potential temperature change is shown in Fig. 4. The vertical gradient of net radiative heating across the BL top resulted in the increasing potential of capping inversion layer and increased convective inhibition, preventing moist convection initiation (Fig. 5). Moreover, a net upper-tropospheric warming in ConstSolarRad is also responsible for stabilized tropospheric column due to the continuous solar shortwave radiation (Figs. 3c, e and 4). It suppresses the convective potential and decreases the depth of the vertical upward motion, and then reduces the latent heat release (Figs. 6b, c) (TZ16). In contrast, net radiative cooling occurred without the solar radiative heating in the NoSolarRad experiment (Fig. 3d), which increased relative humidity and reduced stability between ~3.5–6.5 km in the middle troposphere, enhancing the development potential of deep moist convection (Figs. 4 and 5). Additionally, 12-18 hours of net radiative cooling results in lower potential temperature and greater relative humidity at mid- to upper-levels in NoSolarRad than in ConstSolarRad (Fig. 6a), which further enhances deep moist convection and related latent heat release (Figs. 6b and 6c). The latent heating drives the RMW contraction and intensification, which was especially significant in NoSolarRad from 0600 (66 h) to 1200 UTC 14 September (72 h). After 72 h, high to midlevel clouds increase rapidly with the convection and associated updrafts, with the majority of net radiative cooling located at the top of high clouds (13–15 km) in NoSolarRad (Fig. 3a). The related thermodynamics and dynamics are investigated in the next subsection.

Without solar insolation, NoSolarRad had lower surface air temperatures (Fig. 7a), so after 0000 UTC 14 September, a greater difference between the air and sea surface temperatures results in greater surface fluxes of latent heat and sensible heat, which further decreased convective inhibition and enhanced the WISHE feedback among the surface fluxes, convection, secondary circulation, and accelerated the tangential wind at low-levels (Emanuel 1986) (Figs. 7b-e). It has been found in previous studies that the RI onset of TC was triggered by convective bursts (CBs) in the eyewall, which penetrated into the upper troposphere (Chen and Zhang 2013; Wang and Wang 2014). The impact of the diurnal radiation contrast on CBs is also investigated here. The results were consistent in general, although there have been different definitions of CBs in the literature (e.g. Chen and Zhang 2013; Wang and Wang 2014; Wang and Heng 2016). Therefore, we focus on the results with CBs, which are defined as the grid points where the maximum vertical velocity of at least 5 m s^{-1} between 11 and 15 km. Figure 8 shows that most CBs occurred within 50–160 km radius, with more than one concentrated radial area in NoSolarRad during the period from 1300 UTC 13 Sep (49 h) to 0000 UTC 14 Sep (60 h). ConstSolarRad only had a little difference with NoSolarRad at the above period. However, in NoSolarRad the areal percentage of CBs increased inside 110 km radius and decreased outside of 135 km radius during the period from 0000 (60 h) to 1200 UTC 14 Sep (72 h), which resulted in a quasi-normal distribution peaked at about 75 km radius. The increased CBs inside the radius of about 60 km occurred at not only the downshear-left quadrant but also the upshear-left quadrant (cf. Fig. 10c). The inward shift of CBs with the intensification of TC was consistent with previous observations (e.g. Rogers et al. 2016). In ConstSolarRad, the CBs also increased near the 105 km radius, but decreased inside 70 km radius, which resulted in the much less

CBs inside 90 km than in NoSolarRad. The difference of CBs between the two experiments was relatively smaller at outer core (outside of about 130 km) (Fig. 8), because the convective inhibition was very small at the outer core and convection was easy to develop at the downshear quadrants (Fig. 7e). The detailed process will be shown in next subsection, through which the difference of CB distribution leads to the difference of eyewall contraction between the two experiments.

b. Dynamics of RMW contraction

The radiation-induced difference in convection between the two sensitivity experiments of NoSolarRad and ConstSolarRad influenced both the storm structure and intensity evolution at the stages before RI onset and during RI simultaneously (Fig. 1). From 0000 (60 h) to 1200 UTC 14 September (72 h), the RMW of CNTL and NoSolarRad continued to contract significantly, while that of ConstSolarRad did not continuously contract after 0600 UTC 14 September (66 h) and was greater than in NoSolarRad and CNTL (Fig. 1b). The dynamics of the radiation-induced differences of TC eyewall contraction are analyzed here in detail.

The necessary condition for RMW contraction is the negative radial gradient of the time tendency of tangential wind at the RMW following Stern et al. (2015), i.e. the time tendency of tangential wind is greater inside RMW than that outside. We performed a budget analysis of the tangential wind tendency to address two issues: (1) which processes induced the difference of eyewall contraction between the two experiments, and (2) whether these processes were different between low- and mid-levels, following

$$\frac{\partial \bar{v}}{\partial t} = -\bar{u}(f+\bar{\zeta}) - \bar{w}\frac{\partial \bar{v}}{\partial z} - \overline{u'\zeta'} - \overline{w'\frac{\partial v'}{\partial z}} + \bar{F}, \tag{1}$$

which is the same equation as Eqs. (1) and (2) in T17. The storm-relative radial, tangential, and vertical components of velocity in cylindrical coordinates are given by u, v, and w, respectively. ζ is vertical components of relative vorticity, and f is the Coriolis parameter. z is height. The azimuthal average and the departure from it (or eddy) are denoted by the bar and prime, respectively. The first four terms on the right-hand side of Eq. (1) are the mean radial flux of absolute vertical vorticity, the mean vertical advection of mean tangential wind, the eddy radial vorticity flux, and the eddy vertical advection of tangential wind, respectively. $\bar{F}$ represents the term owing to subgrid-scale processes in the numerical model comprising both diffusive and surface layer processes.

The most distinct difference of the RMW contraction between NoSolarRad and ConstSolarRad occurred from 60 to 72 h (Figs. 1d and 2). The height–radius plot of the tangential velocity budget analysis, averaging between 0000 (60 h) and 1200 UTC 14 Sep (72 h), is shown in Fig. 9. In NoSolarRad, the RMW contracted larger than in ConstSolarRad during the period (Fig. 9). The maximum of tangential wind tendency collocated with the ending RMW (Fig. 9a). The sum of mean radial flux of absolute vertical vorticity and eddy radial vorticity flux contribute greater tangential wind tendency inside the RMW than outside in BL, so it induce the RMW contraction (Fig. 9c). The sum of mean and eddy vertical advection of tangential wind was much smaller around the RMW below 1 km (Fig. 9e). Specifically, the radial eddy vorticity flux contributed greater positive tangential wind tendency inside the RMW than outside (Fig.

9g). Therefore, the process of radial eddy vorticity flux contributed partially to the RMW contraction below about 1 km during the period. In comparison with NoSolarRad, the process of radial vorticity flux also played the same role below about 1 km in ConstSolarRad, although the contribution was smaller (Figs. 9d, h). The other terms did not contribute to RMW contraction positively in BL, either (Figs. 9b, f).

The budget analysis of tangential wind tendency pinpoints that the radial eddy vorticity flux contributes partially to the RMW contraction in low levels. To further identify the cause of different behavior of the eddy vorticity flux in the low-level between the two experiments, the horizontal cross sections of the radial eddy vorticity flux at the height of 250 m averaged between 0000 (60 h) and 1200 UTC 14 September (72 h) were shown for NoSolarRad (Fig. 10a) and ConstSolarRad (Fig. 10d). NoSolarRad (Fig. 10a) shows some stronger positive eddy vorticity flux in the downshear-left quadrant inside the RMW of about 60 km than ConstSolarRad (Fig. 10d). The shear was about 4 m s^{-1} and southwesterly, which was close to the observation (Fig. 2 in Zawislak et al. 2016). The configuration of eddy radial flow and eddy vorticity, which are the two components of eddy vorticity flux, are both crucial to determining the eddy vorticity flux. As can be seen, the maximum positive eddy vorticity and accompanied eddy radial inflow are both stronger in the downshear-left quadrant inside the RMW in NoSolarRad than those in ConstSolarRad (Figs. 10b, e). The stronger eddy vorticity and eddy inflow in NoSolarRad inside RMW were related to more CBs there than in ConstSolarRad (Figs. 10c, f). The deep convection occurring at not only the downshear-left quadrant but also the upshear-left quadrant in NoSolarRad was similar to the observation in the period (Fig. 6 in Zawislak et al. 2016). In contrast, deep convection remained in the downshear quadrant outside of RMW and did not propagate upshear in ConstSolarRad (Fig. 10f), so the TC was less likely to experience RMW contraction and RI. This has been hypothesized in an observational study (Rogers et al. 2016) and modeling study (Leighton et al. 2018).

Which processes dominate the difference of RMW contraction between the two experiments in the mid-levels (~3–9 km)? The mean radial flux of absolute vertical vorticity was very small at mid-levels in both the two experiments before RI onset (Figs. 9c, d). The radial eddy vorticity flux was mostly negative inside of RMW in NoSolarRad and ConstSolarRad (Figs. 9g, h). It is found that the process of the sum of mean and eddy vertical advection of tangential wind contributed significantly to the RMW contraction in the mid-levels in NoSolarRad, because the term is positive and greater inside of the RMW (Fig. 9e). In comparison, the term is smaller in ConstSolarRad although it is positive inside of the RMW (Fig. 9f). The greater vertical advection of tangential wind at the mid-levels inside of RMW in NoSolarRad was related to both the greater vertical updraft and greater low-level tangential wind than that in ConstSolarRad (Figs. 2, 3a, b). The greater vertical updraft in NoSolarRad was directly associated with the more active convection (Figs. 8, 9a, and 10). The greater low-level tangential wind in NoSolarRad was achieved gradually through the stronger symmetric and asymmetric spin-up (Figs. 9c, g), which also benefited from the strengthened convection inside the RMW.

5. Discussion and conclusions

This work examines the sensitivity of RMW contraction of a TC to the diurnal radiation contrast through high-resolution convection permitting full-physics simulations of Hurricane Edouard (2014) using the WRF model. A set of two sensitivity experiments with either endless nighttime (no solar radiative forcing) or endless daytime (persistent maximum solar shortwave forcing) during the early intensification are designed to isolate the varying roles of the diurnal radiation contrast to the RMW contraction. A comparison of the two sensitivity runs shows that the RMW contraction during intensification may be highly sensitive to the diurnal radiation contrast.

The result of ConstSolarRad implies that the shortwave radiative heating over the 12 hours of daytime on the BL top is larger in magnitude than the cooling from the longwave radiation during the early intensification stage of TC, which increases the stability near the BL top and suppresses the development of moist convection. However, the integrated net radiative cooling over 12 hours of nighttime potentially decreases the BL top potential temperature, and increases the development potential of moist convection. Once the deep convection is triggered, the mid- to upper-troposphere is moistened, which is conducive to more active convection and latent heat release (Fig. 6). The enhanced surface fluxes of latent and sensible heating due to the WISHE feedback mechanism will also enlarge the difference in the strength of convective and latent heating inside the RMW between the daytime and nighttime. In the environment of weak vertical shear, most of CBs increased inside of the RMW both in the downshear-left quadrant and upshear-left quadrant with the intensification in NoSolarRad. Conversely, the CBs were less and confined to the downshear quadrant outside of the RMW in ConstSolarRad.

The tropospheric column is constantly stabilized in the ConstSolarRad experiment, due to the solar shortwave radiative heating in the upper-troposphere significantly. It can also curtail the potential and depth of vertical upward motion, and some of the latent heat releasing ultimately. Therefore, the secondary circulation of TC is weakened at the intensification stage. The mechanism is consistent with the previous findings in TZ06 and T17.

The budget calculation of tangential wind tendency reveals that the sum of mean radial flux of absolute vertical vorticity and eddy radial vorticity flux contributes to the RMW contraction during the early intensification in low levels. Inside of the RMW, maximum positive eddy vorticity and accompanied eddy radial inflow induced by deep convection in the downshear-left and upshear-left quadrants resulted in the greater eddy vorticity flux in NoSolarRad. In contrast, the radial eddy vorticity flux was weaker in ConstSolarRad, due to the suppressed convection. The dominant process controlling the RMW contraction in the mid-levels, was the greater positive vertical advection of tangential wind inside of the RMW. In NoSolarRad, the more vigorous convection inside of the RMW not only enhanced the vertical updraft, but also strengthened the low-level tangential wind, and vertical gradient of that between low- and mid-levels consequently. Conversely, the corresponding terms were smaller due to the weaker convection in ConstSolarRad. Therefore, the RMW contracted much less at the low-levels and mid-levels in ConstSolarRad than in NoSolarRad.

In this study, SSTs are mostly unaffected by the imposed permanent changes in radiation that should continuously warm or cool the ocean, which would have increasingly impacts on TC through altering surface fluxes. The current study focuses on the impacts of diurnal radiation contrast to the atmospheric processes only, though there are some influences from the air-sea interaction and feedback through the 1-D ocean mixing layer model and WISHE. The impact of ocean variation due to diurnal radiation contrast on the TC should be further investigated.

The boundary layer and entrainment zone are critical to convection initiation and sensitive to the diurnal radiation cycle, so future work is planned to test how these results depend on different representations of cloud–radiative processes using other pairings of radiation, planetary boundary layer, and microphysics schemes. It is recommended that the diurnal cycle of TC size in terms of the RMW or other metrics need to be investigated further using more observations and simulations. It’s meaningful to further test if the chaotic nature of the atmosphere will influence the robustness of the results (Judt et al.2016; Potvin et al. 2017).

Acknowledgments

The authors thank three anonymous reviewers for their helpful comments and suggestions. This work was supported by the National Key R&D Program of China under grants 2017YFC1501601 and the National Nature Science Foundation of China (Grants 41675054). Computing at the Texas Advanced Computing Center (TACC) is acknowledged.

References

Chen, H., and D.-L. Zhang, 2013: On the rapid intensification of Hurricane Wilma (2005). Part II: Convective bursts and the upper-level warm core. *J. Atmos. Sci.*, **70**, 146–162.

Chen, X., Y. Wang, K. Zhao, and D. Wu, 2017: A numerical study on rapid intensification of Typhoon Vicente (2012) in the South China Sea. Part I: Verification of simulation, storm-scale evolution, and environmental contribution. *Mon. Wea. Rev.*, **145**, 877–898.

Chen, X., Y. Wang, J. Fang, and M. Xue, 2018: A numerical study on rapid intensification of Typhoon Vicente (2012) in the South China Sea. Part II: Roles of inner-core processes. *J. Atmos. Sci.*, **75**, 235–255.

Dudhia, J., 1989: Numerical study of convection observed during the Winter Monsoon Experiment using a mesoscale two dimensional model. *J. Atmos. Sci*., **46**, 3077–3107.

Dunion, J. P., C. D. Thorncroft, and C. S. Velden, 2014: The tropical cyclone diurnal cycle of mature hurricanes. *Mon. Wea. Rev.*, **142**, 3900–3919.

Emanuel, K. A., 1986: An air–sea interaction theory for tropical cyclones. Part I: Steady-state maintenance. *J. Atmos. Sci.*, **43**, 585–605

Grell, G. A., and S. R. Freitas, 2014: A scale and aerosol aware stochastic convective parameterization for weather and air quality modeling. *Atmos. Chem. Phys.*, **14**, 5233–5250.

Hong, S., and J. J. Lim, 2006: The WRF single-moment 6-class microphysics scheme

(WSM6). *J. Korean Meteor. Soc*., **42**, 129–151.

——, Y. Noh, and J. B. Dudhia, 2006: A new vertical diffusion package with an explicit treatment of entrainment processes. *Mon. Wea. Rev.*, **134**, 2318–2341.

Judt, F., S. S. Chen, and J. Berner, 2016: Predictability of tropical cyclone intensity: scale- dependent forecast error growth in high- resolution stochastic kinetic-energy backscatter ensembles. *Quart. J. Roy. Meteor. Soc.*, **142**, 43-57.

Kepert, J. D., 2017: Time and space scales in the tropical cyclone boundary layer, and the location of the eyewall updraft. *J. Atmos. Sci*., **74**, 3305-3323.

Leighton, H., S. Gopalakrishnan, J. Zhang, R. Rogers, Z. Zhang, and V. Tallapragada, 2018: Azimuthal distribution of deep convection, environmental factors and tropical cyclone rapid intensification: A perspective from HWRF ensemble forecasts of Hurricane Edouard (2014). *J. Atmos. Sci*. **75**, 275–295.

Melhauser, C., and F. Zhang, 2014: Diurnal radiation cycle impact on the pregenesis environment of Hurricane Karl (2010). *J. Atmos. Sci.*, **71**, 1241–1259.

Mlawer, E. J., S. J. Taubman, P. D. Brown, M. J. Iacono, and S. A. Clough, 1997: Radiative transfer for inhomogeneous atmosphere: RRTM, a validated correlated-k model for the longwave. *J. Geophys. Res*., **102**, 16663–16682.

Munsell, E. B., F. Zhang, J. A. Sippel, S. A. Braun, and Y. Weng, 2017: Dynamics and predictability of the intensification of Hurricane Edouard (2014). *J. Atmos. Sci.*, **74**, 573–595.

Navarro, E. L., and G. J. Hakim, 2016: Idealized numerical modeling of the diurnal cycle of tropical cyclones. *J. Atmos. Sci*, **73**, 4189–4201.

Navarro, E., G. Hakim, and H. Willoughby, 2017: Balanced response of an axisymmetric tropical cyclone to periodic diurnal heating. *J. Atmos. Sci.*, **74**, 3325–3337.

Nguyen, L. T., J. Molinari, and D. Thomas, 2014: Evaluation of tropical cyclone center identification methods in numerical models. *Mon. Wea. Rev.*, **142**, 4326–4339.

O'Neill, M. E., D. Perez-Betancourt, and A. A. Wing, 2017: Accessible environments for diurnal-period waves in simulated tropical cyclones. *J. Atmos. Sci.*, **74**, 2489–2502.

Pollard, R. T., P. B. Rhines, and R. O. Thompson, 1972: The deepening of the wind-mixed layer. *Geophysical Fluid Dynamics*, **4**, 381–404.

Potvin, C. K., E. M. Murillo, M. L. Flora, and D. M. Wheatley, 2017: Sensitivity of supercell simulations to initial-condition resolution. *J. Atmos. Sci.*, **74**, 5-26.

Powell, M. D., 1990: Boundary layer structure and dynamics in outer hurricane rainbands. Part II: Downdraft modification and mixed layer recovery. *Mon. Wea. Rev.*, **118**, 918–938.

Rogers, R., P. Reasor, and J. Zhang, 2015: Multiscale structure and evolution of Hurricane Earl (2010) during rapid intensification. *Mon. Wea. Rev.*, **143**, 536–562.

——, J. Zhang, J. Zawislak, H. Jiang, G. R. Alvey III,E. J. Zipser, and S. N. Stevenson, 2016: Observations of the structure and evolution of Hurricane Edouard (2014) during intensity change. Part II: Kinematic structure and the distribution of deep convection. *Mon. Wea. Rev.*, **144**, 3355–3376.

Shapiro, L. J., and H. E. Willoughby, 1982: The response of balanced hurricanes to local sources of heat and momentum. *J. Atmos. Sci*., **39**, 378–394.

Skamarock, W. C., and Coauthors, 2008: A description of the Advanced Research WRF version 3. NCAR Tech. Note NCAR/TN-4751STR, 113 pp.

Stern, D. P., J. L. Vigh, D. S. Nolan, and F. Zhang, 2015: Revisiting the relationship between eyewall contraction and intensification. *J. Atmos. Sci*., **72**, 1283–1306.

Stewart, S. R., 2014: Hurricane Edouard (AL062014), 11–19 September 2014. National Hurricane Center Tropical Cyclone Rep., 19 pp. [Available online at http://www.nhc.noaa.gov/data/tcr/AL062014_Edouard.pdf.]

Tang, X., and F. Zhang, 2016: Impacts of the diurnal radiation cycle on the formation, intensity and structure of Hurricane Edouard (2014). *J. Atmos. Sci.*, **73**, 2871–2892.

Tang, X., Z. M. Tan, J. Fang, Y. Q. Sun, and F. Zhang, 2017: Impact of the diurnal radiation cycle on secondary eyewall formation. *J. Atmos. Sci*, **74**, 3079–3098.

Wang, Y., and J. Heng, 2016: Contribution of eye excess energy to the intensification rate of tropical cyclones: A numerical study. *J. Adv. Model. Earth Syst*., **8**, 1953–1968.

Wang, H., and Y. Wang, 2014: A numerical study of Typhoon Megi (2010): Part I: Rapid intensification. *Mon. Wea. Rev*., **124**, 29–48.

Weng, Y.-H., and F. Zhang, 2016: Advances in convection-permitting tropical cyclone analysis and prediction through EnKF assimilation of reconnaissance aircraft observations. *J. Meteor. Soc. Japan*, **94**, 345–358.

Willoughby, H. E., J. A. Clos, and M. G. Shoreibah, 1982: Concentric eye walls, secondary wind maxima, and the evolution of the hurricane vortex. *J. Atmos. Sci.*,

39, 395–411.

Zawislak, J., H. Jiang, G. R. Alvey III, E. J. Zipser, R. F. Rogers, J. A. Zhang, and S. N. Stevenson, 2016: Observations of the structure and evolution of Hurricane Edouard (2014) during intensity change. Part I: Relationship between the thermodynamic structure and precipitation. *Mon. Wea. Rev*., **144,** 3333–3354.

Zhang, F., and Y. Weng, 2015: Predicting hurricane intensity and associated hazards: A five-year real-time forecast experiment with assimilation of airborne Doppler radar observations. *Bull. Amer. Meteor. Soc*., **96**, 25–33.

Figure Captions

Figure 1: (a) Model domain setup, (b) maximum 10-m wind speed (m s^{-1}), (c) tracks and (d) radius of maximum azimuthal-mean 10-m wind speed evolutions for control simulation (red line) and sets of sensitivity experiments (see text for detail, solid/dashed blue lines for NoSolarRad/ConstSolarRad experiments), with comparison of NHC best-track (black line in (b) and (c)) or IBTrACS data (black line in (d)). The period is from 1200 UTC 11 September (0 h) to 1800 UTC 16 September 2014 (126 h). The circles on the tracks denote the location every 6 h. The gray dashed line denotes the RI onset in the control run and NoSolarRad roughly.

Figure 2: Hovmöller plots of azimuthal-mean tangential velocity (contour; m s^{-1}) and vertical velocity (shading) at heights of (a) 7 km and (c) 2 km for NoSolarRad. (b) and (d) are as (a) and (c), but for ConstSolarRad. The period is from 1800 UTC 13 September (54 h) to 1200 UTC 16 September 2014 (120 h). The superposed black lines denote the RMW. The tangential and vertical wind field were filtered in time to remove scales less than 6 hours.

Figure 3: Height–time plot of (a) cloud fraction (shading), vertical velocity (contour intervals are 0.2 m s^{-1}), (d) net radiative heating averaged between 30- and 90-km radius from 1300 UTC 13 September (49 h) to 1800 UTC 16 September 2014 (126 h) for NoSolarRad. (b) and (e) are as (a) and (d), but for ConstSolarRad. (c) Shortwave and (f) longwave radiative heating for ConstSolarRad are also shown. The yellow boxes denote the especially focused periods and heights.

Figure 4: Potential temperature change from net radiation averaged between 30- and

90-km radius from 1200 UTC 13 September (48 h) to 0600 UTC 14 September 2014 (66 h).

Figure 5: Low-level lapse rate averaged between 30- and 90-km radius from 0600 (66 h) to 0900 UTC 14 September 2014 (69 h).

Figure 6: Height–time plot of NoSolarRad minus ConstSolarRad difference of (a) relative humidity (unit: %), (b) vertical velocity (unit: m s^{-1}) and (c) latent heating (unit: 10^{-3} K s^{-1}) averaged between 30- and 90-km radius from 1300 UTC 13 September (49 h) to 1200 UTC 14 September 2014 (72 h).

Figure 7: Evolution of (a) 2-m temperature, (b) 10-m wind speed, surface fluxes of (c) latent heat and (d) sensible heat, (e) convective inhibition averaged between 30- and 90-km radius (black) for NoSolarRad (solid) and ConstSolarRad (dashed) from 1200 UTC 13 September (48 h) to 1200 UTC 15 September 2014 (96 h). Red lines are for between 90- and 240-km radius.

Figure 8: The areal percentage (%) of CBs binned every 9 km of radius, averaged during two periods for NoSolarRad (solid) and ConstSolarRad (dashed), from 1300 UTC 13 September (49 h) to 0000 UTC 14 September (60 h) (black), and from 0000 (60 h) to 1200 UTC 14 September 2014 (72 h) (red), respectively.

Figure 9: Height–radius plots of (a) tangential wind tendency directly from the model output (blue contours; interval 10^{-4} m s^{-2}), radial [red contours; interval 1 m s^{-1}; solid (dashed) lines denote positive (negative) values] and vertical (shading) component of wind, (c) sum of radial mean absolute vorticity flux and eddy vorticity flux, (e) sum of mean and eddy vertical advection of tangential wind, and (g) radial eddy vorticity flux

for NoSolarRad, averaged azimuthally between 0000 (60 h) and 1200 UTC 14 September 2014 (72 h). (b)-(h) are as (a)-(g), but for ConstSolarRad. The superposed green lines denote the RMW at 0000 UTC (60 h; solid) and 1200 UTC 14 September 2014 (72 h; dashed), respectively.

Figure 10: (a) radial eddy vorticity flux (10^{-4} m s^{-2}), (b) eddy radial component of storm-relative flow (vectors) and eddy vorticity (shading, 10^{-5} s^{-1}), (c) storm-relative flow (vectors) and vorticity (shading; 10^{-5} s^{-1}) at the height of 250 m, averaged between 0000 (60 h) and 1200 UTC 14 September 2014 (72 h) for NoSolarRad. Yellow arrows denote vertical shear vectors of averaged environmental wind. Green dots denote the grid points where CBs occurred. (b)-(f) are as (a)-(e), but for ConstSolarRad. The black circles are centered over the storm center with radii of 30 and 60 km.

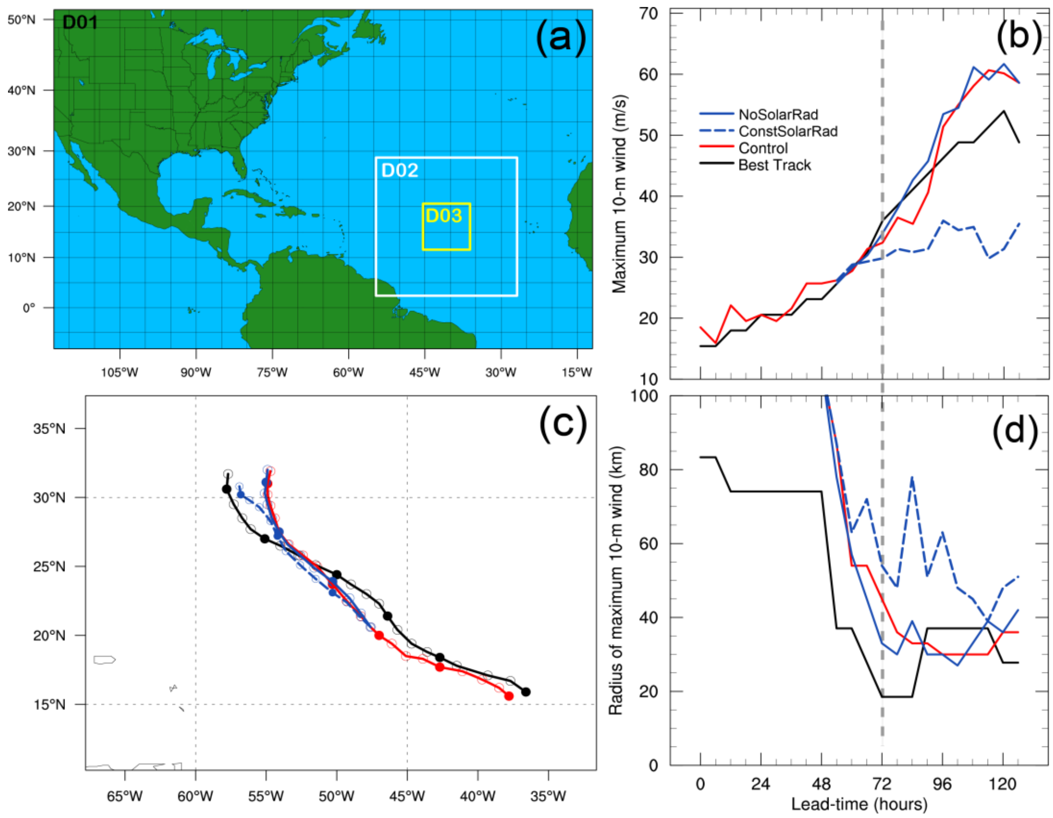

Figure 1: (a) Model domain setup, (b) maximum 10-m wind speed (m s^{-1}), (c) tracks and (d) radius of maximum azimuthal-mean 10-m wind speed evolutions for control simulation (red line) and sets of sensitivity experiments (see text for detail, solid/dashed blue lines for NoSolarRad/ConstSolarRad experiments), with comparison of NHC best-track (black line in (b) and (c)) or IBTrACS data (black line in (d)). The period is from 1200 UTC 11 September (0 h) to 1800 UTC 16 September 2014 (126 h). The circles on the tracks denote the location every 6 h. The gray dashed line denotes the RI onset in the control run and NoSolarRad roughly.

494

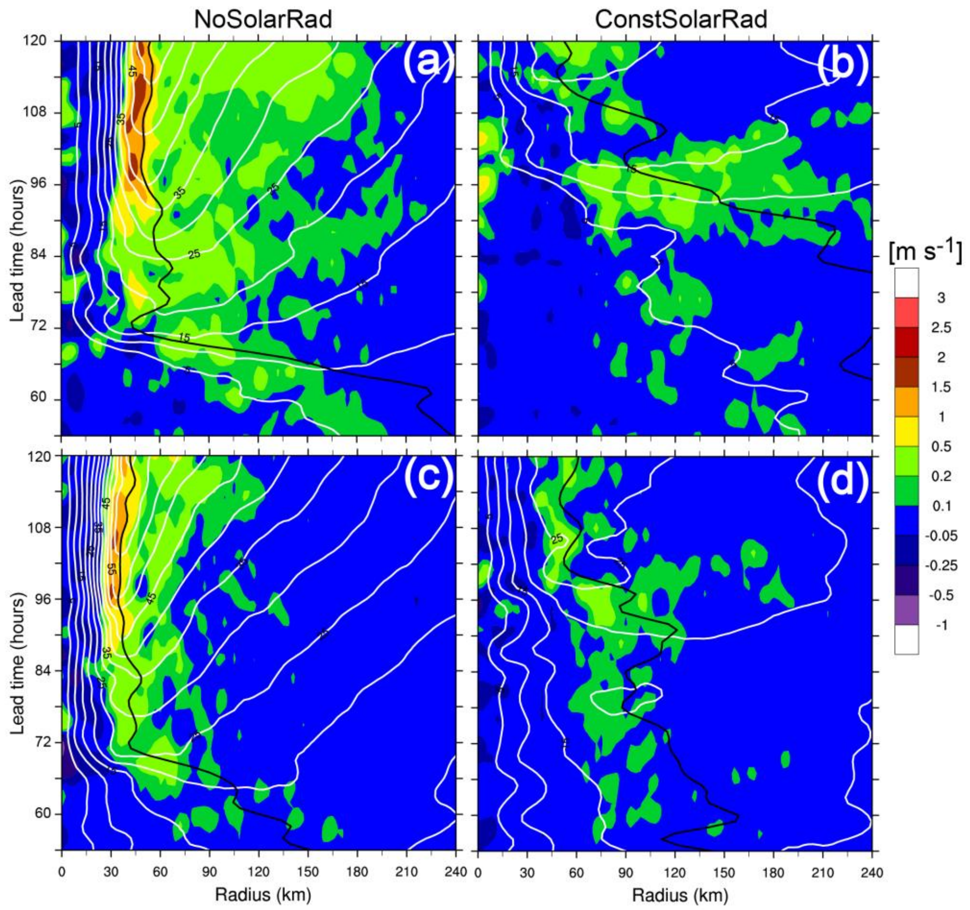

Figure 2: Hovmöller plots of azimuthal-mean tangential velocity (contour; m s^{-1}) and vertical velocity (shading) at heights of (a) 7 km and (c) 2 km for NoSolarRad. (b) and (d) are as (a) and (c), but for ConstSolarRad. The period is from 1800 UTC 13 September (54 h) to 1200 UTC 16 September 2014 (120 h). The superposed black lines denote the RMW. The tangential and vertical wind field were filtered in time to remove scales less than 6 hours.

495

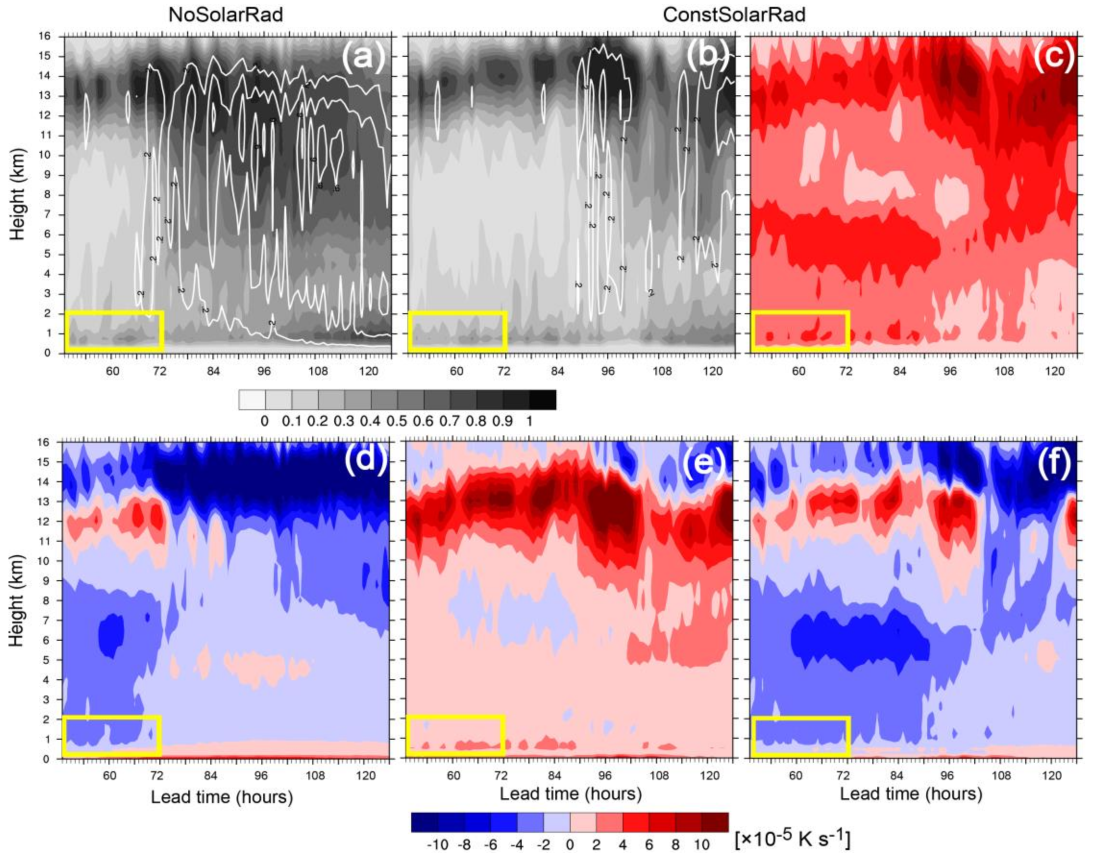

Figure 3: Height–time plot of (a) cloud fraction (shading), vertical velocity (contour intervals are 0.2 m s^{-1}), (d) net radiative heating averaged between 30- and 90-km radius from 1300 UTC 13 September (49 h) to 1800 UTC 16 September 2014 (126 h) for NoSolarRad. (b) and (e) are as (a) and (d), but for ConstSolarRad. (c) Shortwave and (f) longwave radiative heating for ConstSolarRad are also shown. The yellow boxes denote the especially focused periods and heights.

496

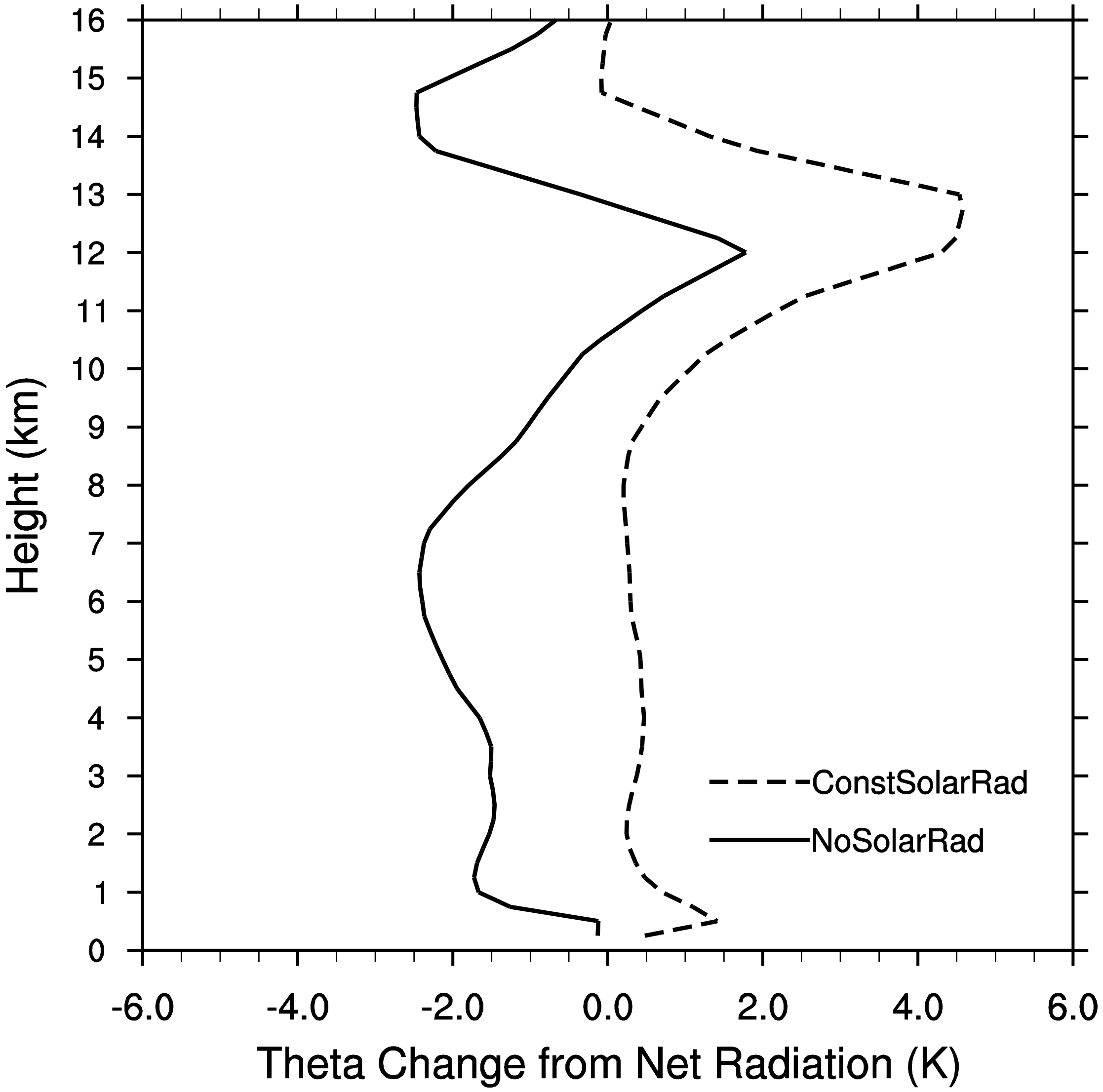

Figure 4: Potential temperature change from net radiation averaged between 30- and 90-km radius from 1300 UTC 13 September (48 h) to 0600 UTC 14 September 2014 (66 h).

497

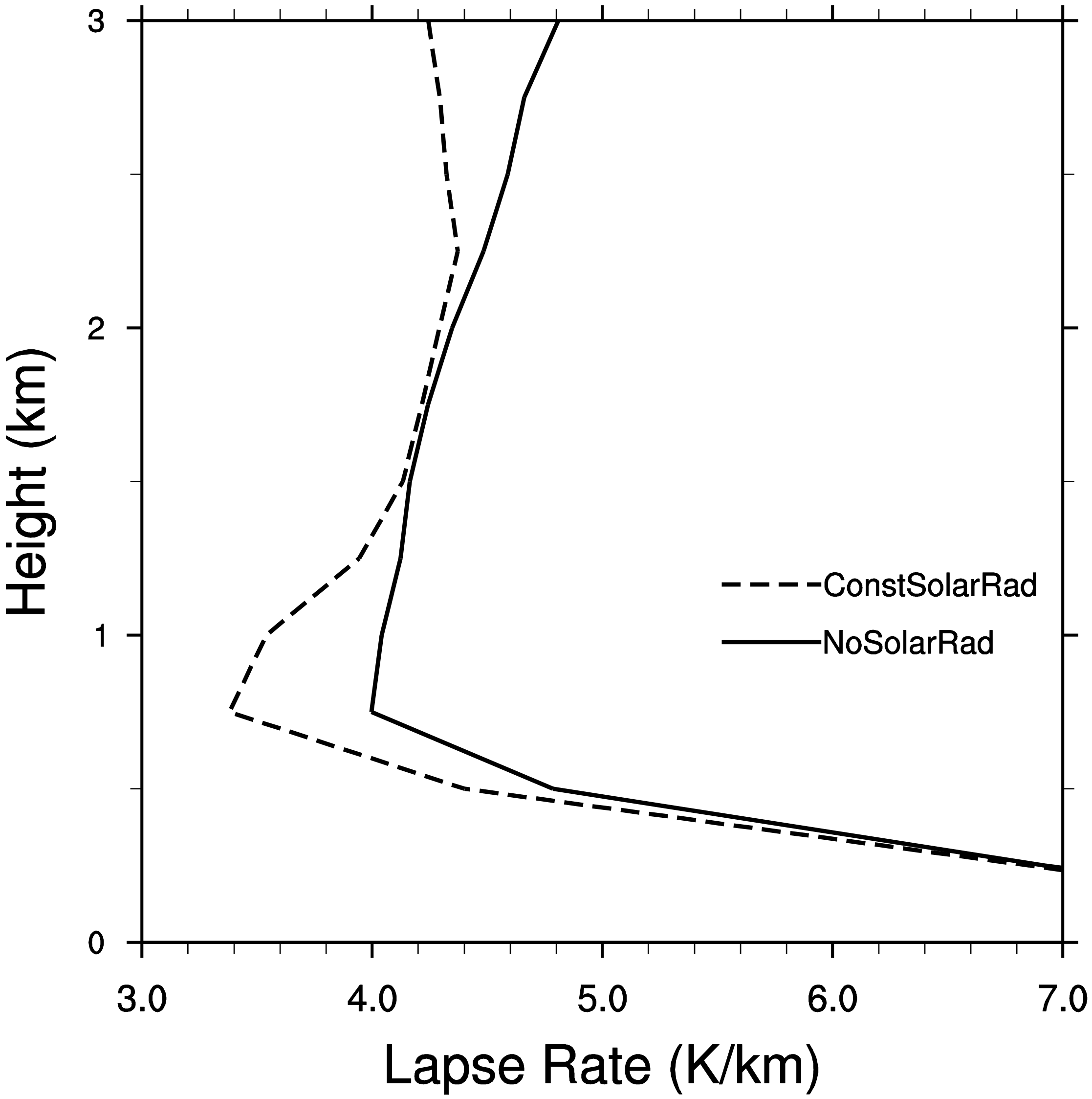

Figure 5: Low-level lapse rate averaged between 30- and 90-km radius from 0600 (66 h) to 0900 UTC 14 September 2014 (69 h).

498

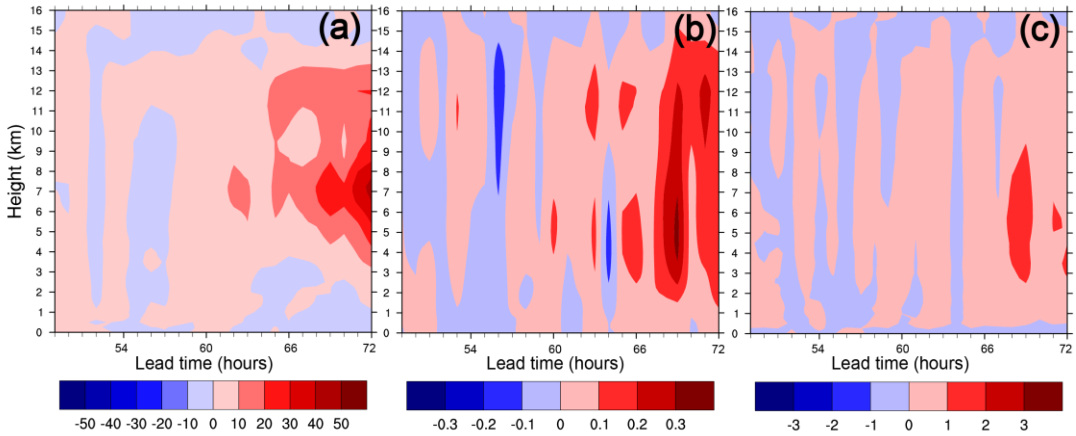

Figure 6: Height–time plot of NoSolarRad minus ConstSolarRad difference of (a) relative humidity (unit: %), (b) vertical velocity (unit: m s^{-1}) and (c) latent heating (unit: 10^{-3} K s^{-1}) averaged between 30- and 90-km radius from 1300 UTC 13 September (49 h) to 1200 UTC 14 September 2014 (72 h).

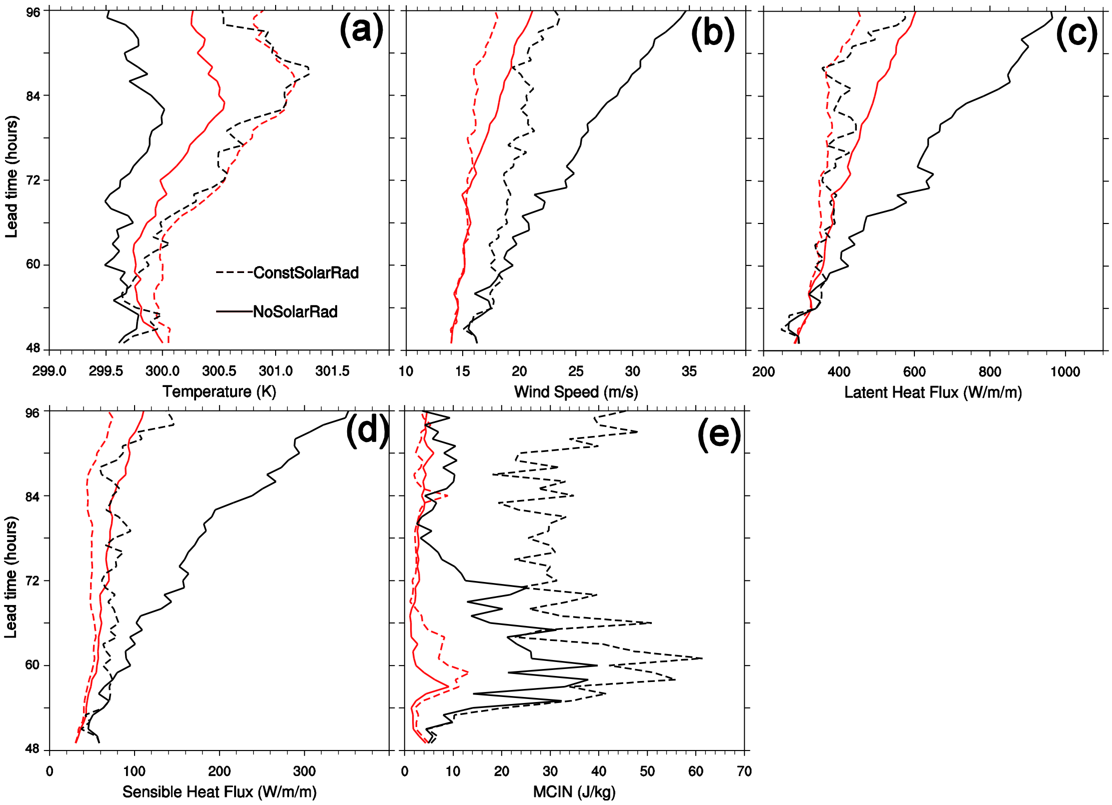

Figure 7: Evolution of (a) 2-m temperature, (b) 10-m wind speed, surface fluxes of (c) latent heat and (d) sensible heat, (e) convective inhibition averaged between 30- and 90-km radius (black) for NoSolarRad (solid) and ConstSolarRad (dashed) from 1200 UTC 13 September (48 h) to 1200 UTC 15 September 2014 (96 h). Red lines are for between 90- and 240-km radius.

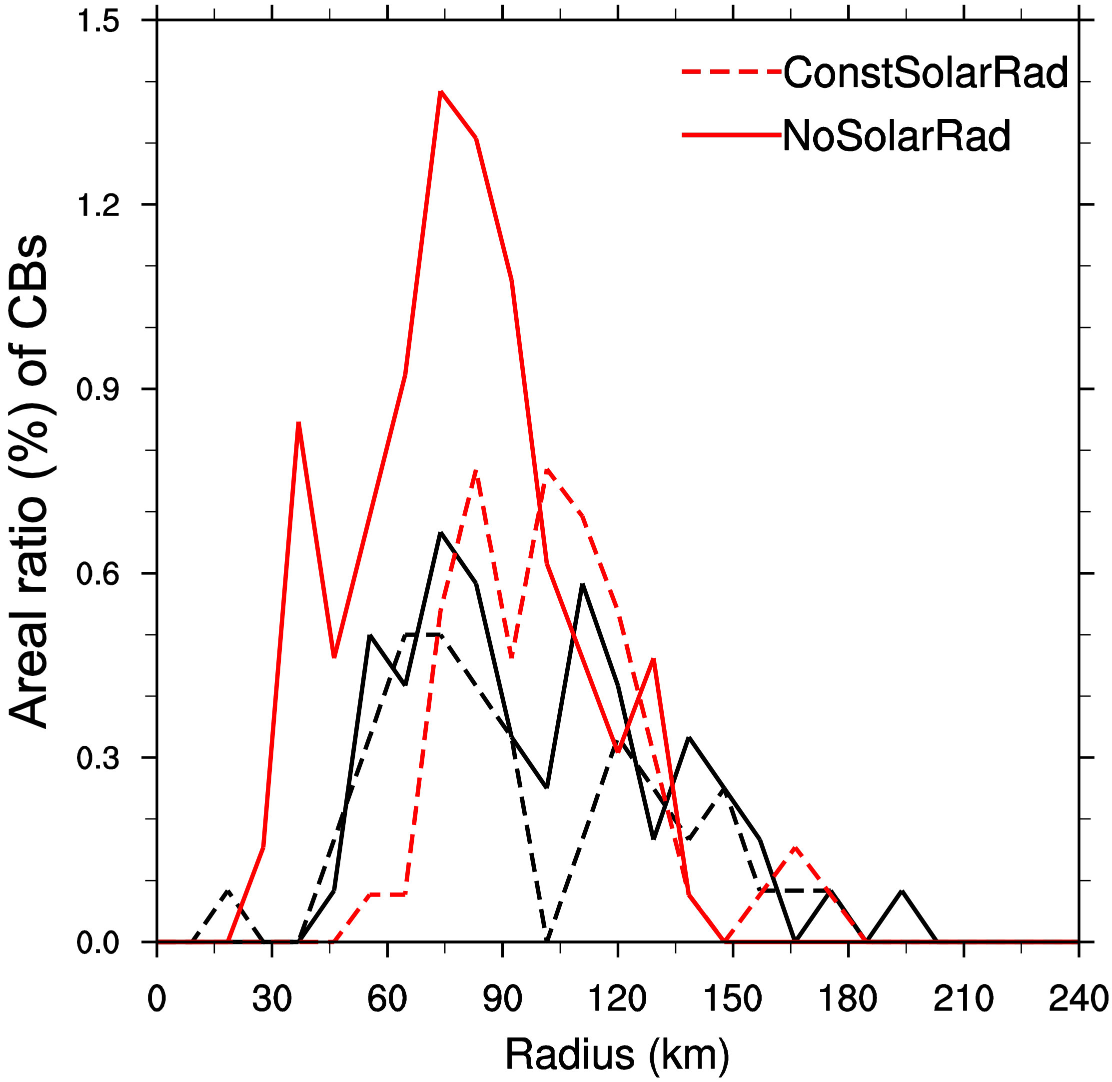

Figure 8: The areal percentage (%) of CBs binned every 9 km of radius, averaged during two periods for NoSolarRad (solid) and ConstSolarRad (dashed), from 1300 UTC 13 September (49 h) to 0000 UTC 14 September (60 h) (black), and from 0000 (60 h) to 1200 UTC 14 September 2014 (72 h) (red), respectively.

501

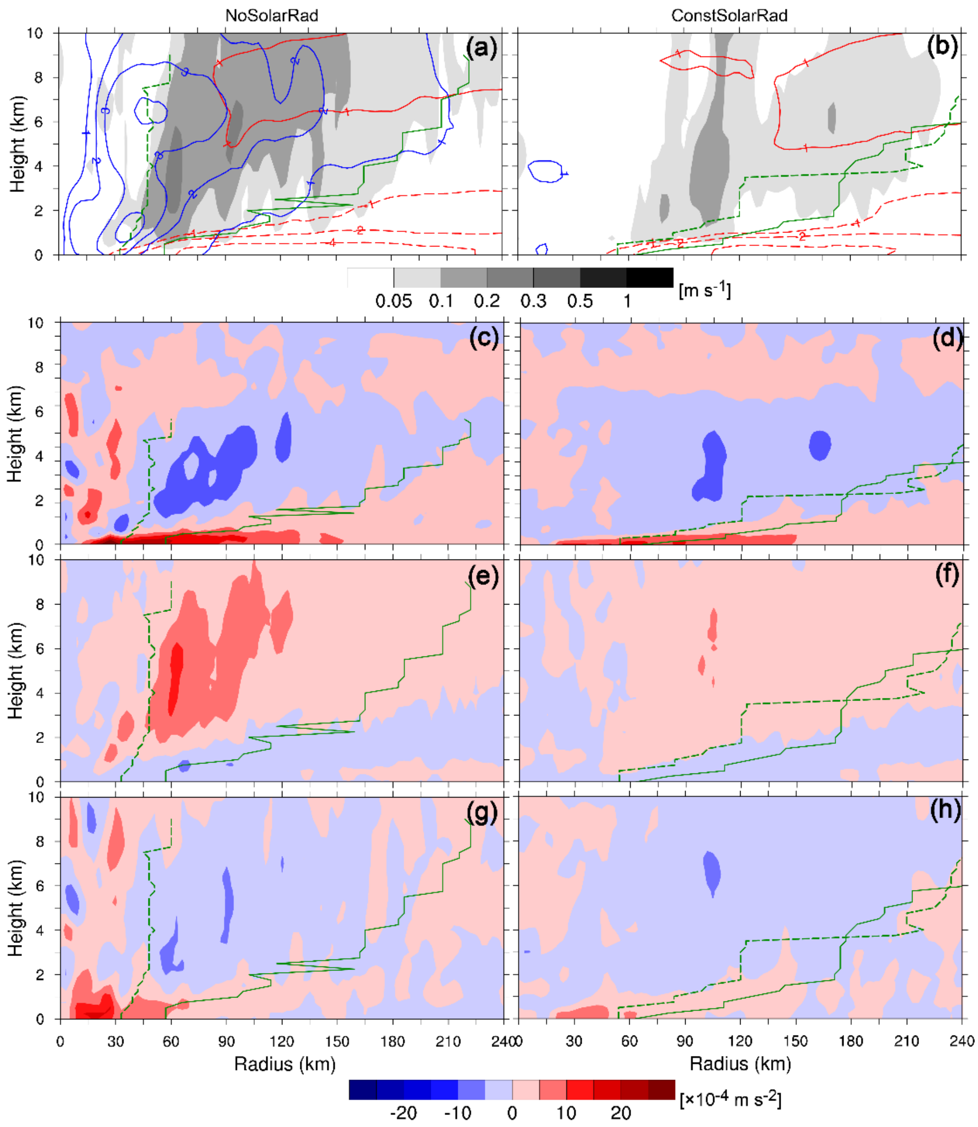

Figure 9: Height–radius plots of (a) tangential wind tendency directly from the model output (blue contours; interval 10^{-4} m s^{-2}), radial [red contours; interval 1 m s^{-1}; solid (dashed) lines denote positive (negative) values] and vertical (shading) component of wind, (c)sum of radial mean absolute vorticity flux and eddy vorticity flux, (e) sum of mean and eddy vertical advection of tangential wind, and (g) radial eddy vorticity flux for NoSolarRad, averaged azimuthally between 0000 (60 h) and 1200 UTC 14 September 2014 (72 h). (b)-(h) are as (a)-(g), but for ConstSolarRad. The superposed green lines denote the RMW at 0000 UTC (60 h; solid) and 1200 UTC 14 September 2014 (72 h; dashed), respectively.

502

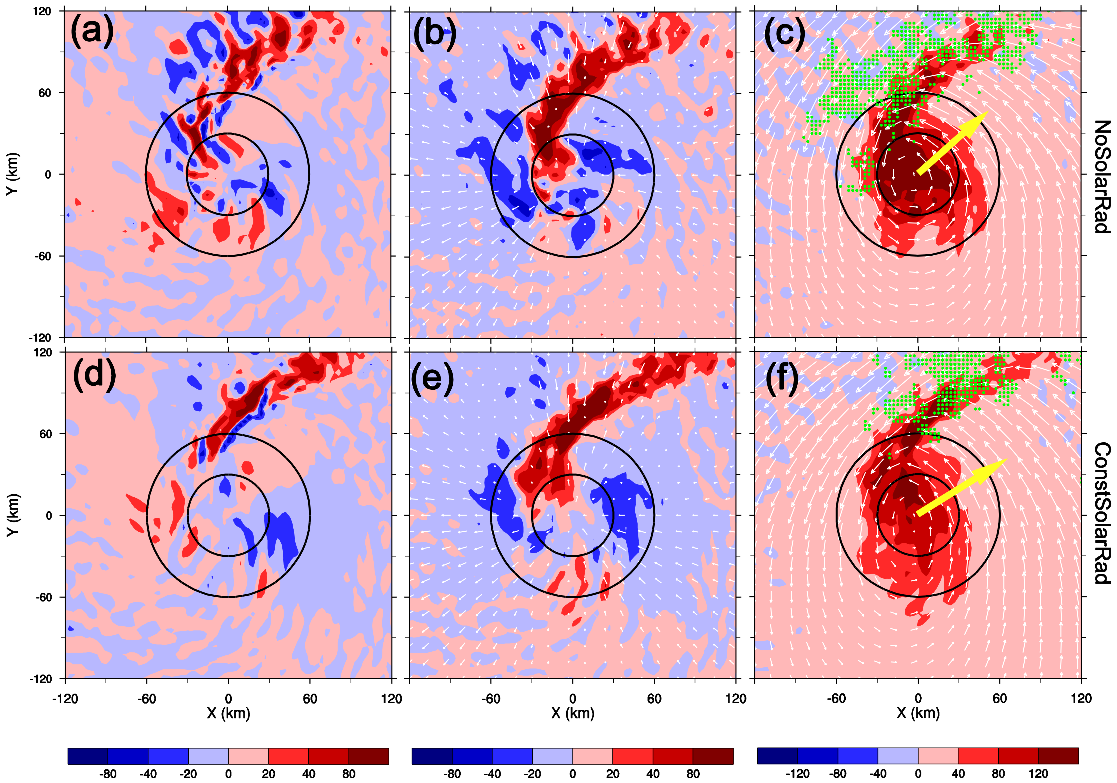

Figure 10: (a) radial eddy vorticity flux (10^{-4} m s^{-2}), (b) eddy radial component of storm-relative flow (vectors) and eddy vorticity (shading, 10^{-5} s^{-1}), (c) storm-relative flow (vectors) and vorticity (shading; 10^{-5} s^{-1}) at the height of 250 m, averaged between 0000 (60 h) and 1200 UTC 14 September 2014 (72 h) for NoSolarRad. Yellow arrows denote vertical shear vectors of averaged environmental wind. Green dots denote the grid points where CBs occurred. (b)-(f) are as (a)-(e), but for ConstSolarRad. The black circles are centered over the storm center with radii of 30 and 60 km.

503